March 1991

Long-Range Dipole Field Effects on H^- Detachment Processes above the H(n=2) Threshold

Anthony F. Starace
University of Nebraska-Lincoln, astarace1@unl.edu

Invited talk presented at the **Third U.S.–Mexico Atomic and Molecular Physics Symposium**, Cocoyoc, Mexico, 13–16 March 1991. (World Scientific Publishing Co., In press)

LONG-RANGE DIPOLE FIELD EFFECTS ON H^- DETACHMENT PROCESSES ABOVE THE H(n=2) THRESHOLD

ANTHONY F. STARACE
Department of Physics and Astronomy
The University of Nebraska
Lincoln, NE 68588-0111

ABSTRACT

The long-range dipole field interaction between a low energy electron and the hydrogen atom in the n = 2 state is shown to be the key for understanding significant features of a number of H^- detachment processes. Collisional, single photon, and two-photon detachment processes are examined, each of which is shown to be sensitive to different aspects of low-energy H(n=2)–e^- interactions. Specifically, these detachment processes are best suited respectively for exhibiting the finite threshold cross sections for certain $^1S^e$, $^1P^o$, and $^1D^e$ final-state channels, the shape resonance in one of the $^1P^o$ final state channels, and the near–threshold Galitis—Damburg oscillations in certain $^1S^e$ and $^1D^e$ final state channels. The latter oscillations have yet to be observed experimentally in any process.

1. Introduction

This paper is focused on processes involving the detachment of the H^- ion and the simultaneous excitation of the resulting H atom to its n=2 state. The processes we shall discuss are quite different from one another and involve different experimental technologies. They are high energy collisional detachment, photodetachment, and two-photon detachment, i.e.,

$$H^- + T \rightarrow H(n=2) + e^- + T^* \quad (1)$$

$$H^- + \gamma \rightarrow H(n=2) + e^- \quad (2)$$

$$H^- + 2\gamma \rightarrow H(n=2) + e^- \quad . \quad (3)$$

In Eq. 1, T denotes an atomic target atom and the asterisk on the right hand side of Eq. 1 denotes that this target atom may be in either its initial state, an excited bound state, or an ionized state as a result of the collision. (Typically, the final state of the target in collisional detachment processes is not measured experimentally.)

The aim of this paper is to show that key features of the very different detachment processes in Eqs. 1–3 may be understood from a unified point of view. This point of view has as its focus the low energy states of the fundamental H(n=2) – e^- three-body system. It will be shown that each of the processes in Eqs. 1–3 is ideally suited for exhibiting different aspects of these low energy states.

In what follows, we discuss first the low-energy states of the H(n=2) – e^- three-body system, using an adiabatic hyperspherical representation.[1] We then examine how these states affect each of the detachment processes in Eqs. 1–3 in turn. Readers interested in further details of the theoretical work (i.e., on collisional detachment[2–4] and on one- and two-photon detachment[5] processes) upon which the present paper is based are referred to recent publications of the author and his collaborators.[2–5] These publications should also be consulted for more complete references to related experimental and theoretical work by others.

2. Low-Energy States of the H(n=2) – e^- System

In our calculations we describe the H(n=2) – e^- three-body system in an adiabatic hyperspherical representation[1,6,7] since this is known to describe fairly accurately the key dynamical features of this system[8] and since this representation is known to diagonalize asymptotically the long-range dipole interaction for this system.[1,8]

In the hyperspherical approach the exact two-electron wave function $\psi(\mathbf{r}_1,\mathbf{r}_2)$ is expanded in a complete set of adiabatic eigenfunctions $\phi_\mu(R,\alpha,\hat{\mathbf{r}}_1,\hat{\mathbf{r}}_2)$, which depend parametrically on a hyperradius $R \equiv (r_1^2+r_2^2)^{1/2}$ and are functions of the five angular variables $\alpha \equiv \tan^{-1}(r_2/r_1)$, $\hat{\mathbf{r}}_1$ and $\hat{\mathbf{r}}_2$.

$$\psi(R,\alpha,\hat{\mathbf{r}}_1,\hat{\mathbf{r}}_2) \equiv (R^{5/2}\sin\alpha\cos\alpha)^{-1}\sum_\mu F_\mu(R)\,\phi_\mu(R,\alpha,\hat{\mathbf{r}}_1,\hat{\mathbf{r}}_2)\ . \qquad (4)$$

The ϕ_μ satisfy an angular equation[1,6,7] having eigenvalue $U_\mu(R)$. The F_μ satisfy a set of coupled radial equations[1,6,7]; however, in the adiabatic approximation all but the diagonal coupling matrix elements are dropped so that each $F_\mu(R)$ satisfies a one-dimensional radial Schrödinger equation,

$$\left[\frac{d^2}{dR^2} - V_\mu(R) + k^2\right] F_{\mu k}(R) = 0 . \tag{5}$$

In Eq. 5 the effective radial potential $V_\mu(R)$, which characterizes the dynamical features of a particular hyperspherical channel μ converging to the nth level of the H atom is defined by

$$- V_\mu(R) \equiv \frac{U_\mu(R) + \frac{1}{4}}{R^2} + \left(\phi_\mu, \frac{d^2\phi_\mu}{dR^2}\right) - \frac{1}{n^2} , \tag{6}$$

where $(\phi_\mu, d^2\phi_\mu/dR^2)$ is the R-dependent diagonal coupling matrix element for the μth channel. Since the long-range dipole interaction due to the degeneracy of the H(n=2) states[9] is diagonal in the hyperspherical representation,[1,8] the asymptotic form of the effective radial potential is

$$V_\mu(R) \underset{R \to \infty}{\sim} \lambda_\mu(\lambda_\mu + 1)/R^2 . \tag{7}$$

In Eq. 7 λ_μ is an effective orbital angular momentum, which may be real or complex depending on the channel μ. For channels μ in which the long-range dipole interaction[9] is repulsive at asymptotic distances, λ_μ is real. Hence at threshold the cross section for any excitation to the channel μ is zero since it depends on $| k^{\lambda_\mu + 1/2}|^2$, which is zero for $k \to 0$. On the other hand, for channels μ in which the long-range dipole interaction[9] is attractive at asymptotic distances, one may write quite generally,[10]

$$\lambda_\mu = -\frac{1}{2} + i\alpha_\mu \tag{8}$$

As a consequence,the threshold value of the cross section for any excitation to the channel μ is finite[11] since it depends on $|k^{\lambda_\mu+1/2}|^2 = 1$. In addition, as noted by Gailitis and Damburg,[11] the transition matrix elements for channels having complex λ_μ are influenced above threshold by the term $k^{\lambda_\mu+1/2} = k^{i\alpha\mu}$ (cf. Eq. 8), which, when re-written as exp ($i\alpha_\mu$ ln k), may be seen to oscillate as a function of ln k.

The effective potentials $V_\mu(R)$ which converge asymptotically to the H(n=2) threshold and which are most relevant for the detachment processes in Eqs. 1–3 are shown in Fig. 1. All of the $^1S^e$ and $^1P^o$ potential curves are shown as well as the most important $^1D^e$ potential curve. Since the total orbital and spin angular momenta are insufficient to specify the potential curves uniquely, additional specification is necessary. In Fig. 1 we have employed abbreviated labels corresponding to Lin's classification of doubly excited states.[12]

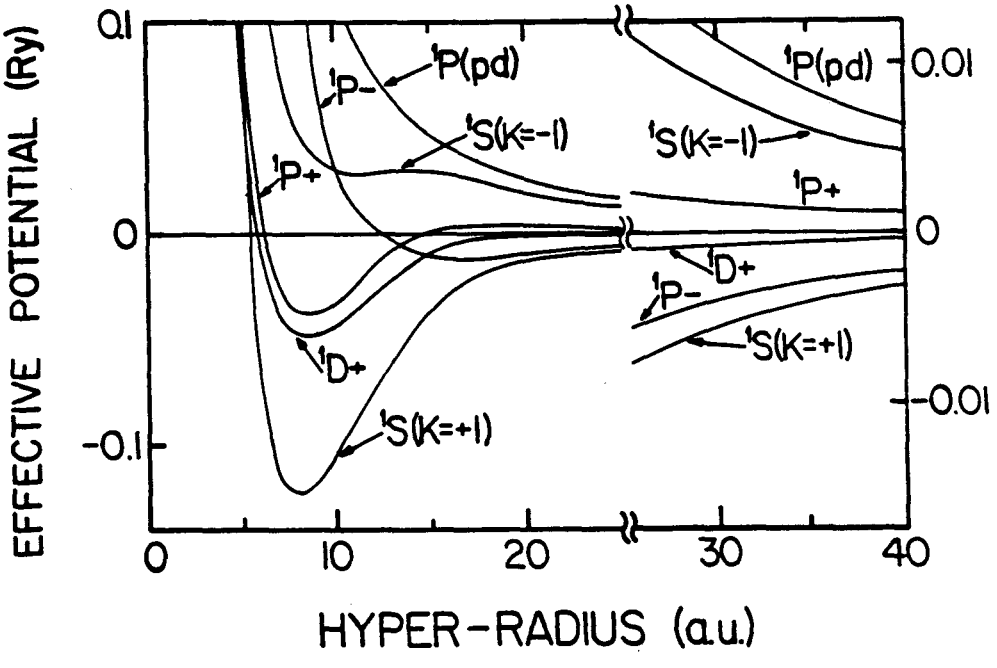

FIG. 1. Effective radial hyperspherical potentials V_μ in Ry plotted vs the hyperradius R for six channels converging to H(n=2): $^1S(K=\pm 1)$, $^1P\pm$, $^1P(pd)$, and $^1D+$. Note that the zero of energy is chosen to be the H(n=2) threshold and that near R = 25 the vertical energy scale is changed.

Note finally that the adiabatic $^1P+$ and $^1P-$ curves have a sharply avoided crossing near R ≈ 13.3 a.u., implying a very strong interaction between them at this value of R. Following others,[1,8,12] we take this strong interaction into account by replacing the adiabatic potentials by the corresponding diabatic potentials (which cross near R ≈ 13.3 a.u.) and ignore any residual interaction between the potentials. We emphasize that this use of the diabatic approximation is limited to these two potentials. All of the other potentials (as well as the $^1P+$ and $^1P-$ potentials outside the R ≈ 13.3 a.u. region) are calculated by solving the adiabatic hyperspherical equations.

The key features of the interactions within the H(n=2) – e^- system are clearly exhibited in the effective potential curves shown in Fig. 1. These are, first, that the $^1P+$ potential is attractive at short distances and weakly repulsive at large distances thereby giving rise to a shape resonance (which is seen experimentally at about 18 meV above threshold).[8] This shape resonance feature dominates the cross section of any process which populates the $^1P^o$ final state channels above the H(n=2) threshold.

Second, because of their long-range repulsive behavior, the $^1P+$, $^1P(pd)$, and $^1S(K = -1)$ potentials all have zero cross sections at threshold.

Third, the three potentials corresponding to the $^1S(K=+1)$, $^1P-$, and $^1D+$ channels are attractive at asymptotic distances. As discussed above, they therefore have complex effective angular momenta. Hence the excitation cross section for each of these channels is finite at threshold (within the center-of-mass frame of the H(n=2) – e^- system). Futhermore, the transition amplitudes for excitations to these three channels having complex effective angular momenta oscillate on a ln k scale above threshold.[11]

In what follows we shall examine each of the processes in Eqs. 1–3 in turn in order to show how these key features of the interactions within the H(n=2) – e^- system are manifested both experimentally and theoretically.

3. Collisional Detachment of H^-

The cross sections for high-energy H^- detachment collisions, particularly those differential in the energy and angle of the detached electron, depend sensitively on the low-energy states of the fundamental $H–e^-$ three-body system. These low-energy states in the H^- frame are related kinematically to the small–angle (i.e., forward-direction) behavior of the detachment cross section measured in the laboratory. The closer to threshold in the H^- frame that one wishes to probe, the closer in angle to the forward direction one must measure. These same kinematic relations, furthermore, magnify the energy scale over which the fundamental dynamics of the $H–e^-$ system may be observed: e.g., for 0.5–MeV H^- detachment collisions, features in the H^- frame measured on a scale of tens of meV appear in the laboratory frame on a scale of tens of eV.

It is useful to examine how each of the final state channels for the $H(n=2) – e^-$ system contribute individually to the doubly differential cross section (DDCS) for the following collisional detachment process:

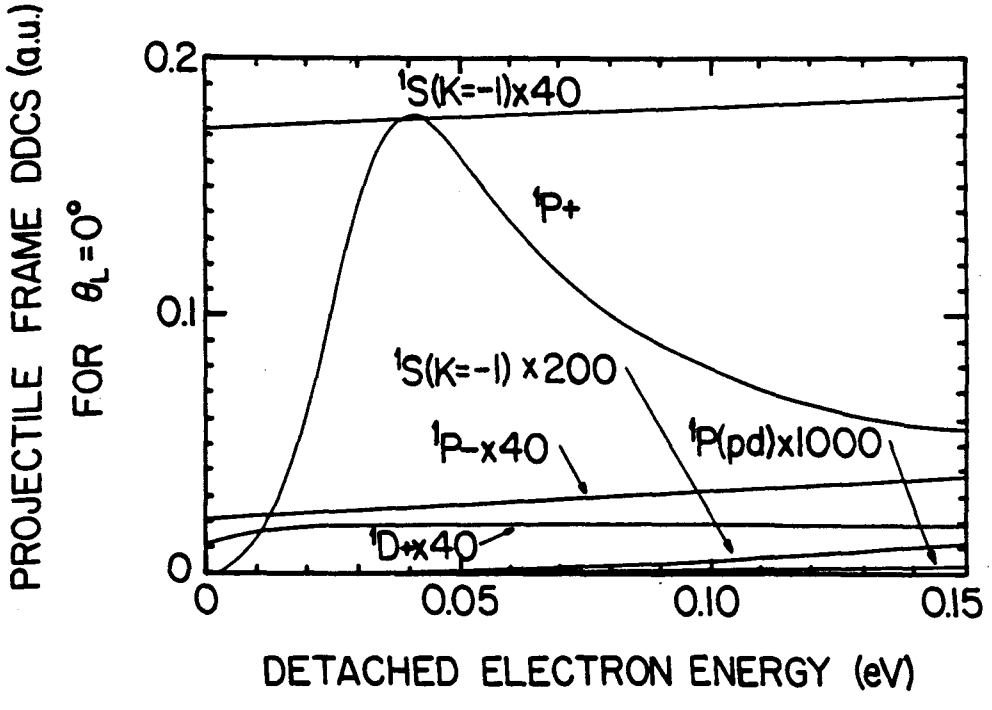

FIG. 2. Projectile–frame DDCS's of Liu and Starace (Ref. 2) for the process 0.5 MeV H^- + He → H(n=2) + e^- + He* for electrons detached at $\theta_P = 0°$, for each of the six hyperspherical channels $^1S(K = \pm 1)$, $^1P_\pm$, $^1P(pd)$, and $^1D_+$ taken separately, plotted vs electron energy.

$$0.5\text{–MeV } H^- + He \rightarrow H(n=2) + e^- + He^* \ . \qquad (9)$$

The asterisk on the right–hand side of Eq. 9 indicates that the He atom may be either in an excited state, bound or continuum, or in the unexcited ground state. The projectile frame DDCS's for electrons detached in the forward direction ($\theta_P = 0°$) are shown in Fig. 2 in the theoretical approximation that each final state channel is treated separately (i.e., incoherently rather than coherently). One sees from Fig. 2 that the $^1P+$ shape resonance channel dominates the collisional detachment process near threshold except for the region right at threshold. At threshold the cross sections for channels having asymptotic repulsive potentials are all zero. In contrast, the cross sections for the three channels having asymptotic attractive potentials are finite at threshold. Fig. 2 shows DDCS results calculated for a He target, but it is typical of results one obtains for any rare gas target. We examine now how the features shown in the projectile frame in Fig. 2 appear in the laboratory frame in actual experimental measurements.

In Fig. 3 we compare our laboratory frame DDCS's with experimental data of Duncan and Menendez[13] for the process,

$$0.5\text{–MeV } H^- + Ar \rightarrow H^* + e^- + Ar^*, \qquad (10)$$

for three laboratory–frame detachment angles. The experimental measurements did not determine the final state of the H atom, which fact is indicated by the asterisk on the right hand side of Eq. 10. Our theoretical calculations[4] were carried out for both H(n=1) and H(n=2) final states. Clearly the large DDCS for the H(n=2) final state is a major feature of the experimental data. In our calculations this feature is shown to be due to the $^1P+$ shape resonance. For small angles θ_L it is clear that the shape resonance must be taken into account in order to achieve good agreement with the experimental data. For larger angles θ_L, the kinematics of the transformation from the projectile frame to the laboratory frame results in progressively less contribution of the $^1P+$ shape resonance to the H(n=2) cross section for the process in Eq. 10.

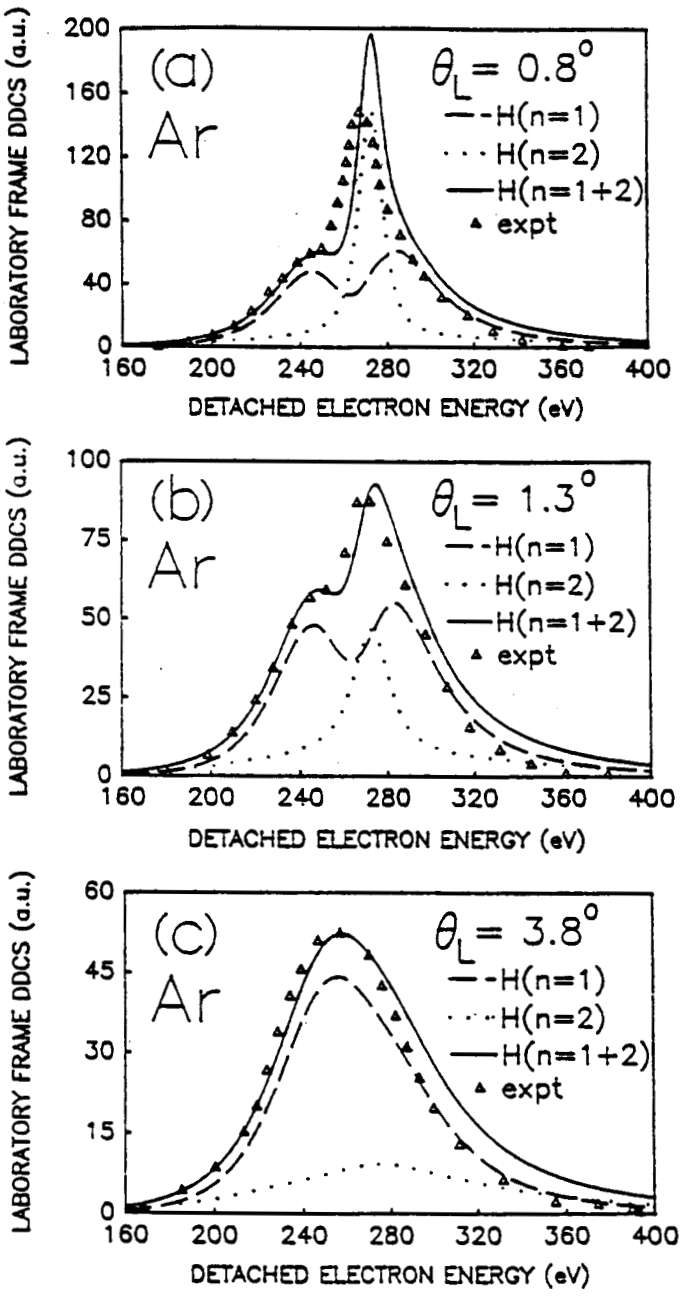

FIG. 3. Laboratory–frame DDCS's for the process 0.5 MeV H^- + Ar → H* + e^- + Ar* for electron–detachment angles of (a) θ_L = 0.8°, (b) θ_L = 1.3°, and (c) θ_L = 3.8°. Theoretical results of Liu and Starace (Ref. 4) are indicated as follows: Dashed curves, results for H(n=1) final states; dotted curves, results for H(n=2) final states; solid curves, sum of H(n=1) and H(n=2) results. Experimental results of Duncan and Menendez (Ref. 13) are indicated by triangles; they are normalized to the solid curves at the position of the lower–energy peak for θ_L = 0.8° and 1.3° and at the position of the single peak for θ_L = 3.8°.

In order to exhibit the fact that three channels of the H(n=2) – e^- system have finite cross sections at threshold in the projectile frame (cf. Fig. 2), one must measure the detached electrons in the laboratory at or very close to $\theta_L = 0°$. One experiment which has done this is that of Anderson, Bangsgaard, and Sørensen[14] for the process,

$$0.1\text{–MeV } H^- + Xe \rightarrow H(n=2) + e^- + Xe^* \ . \qquad (11)$$

Their results are shown in Fig. 4 in comparison with our theoretical results[4] for this process. The sharp cusp feature in both the experimental and theoretical results is the earmark of the finite threshold cross sections in the projectile frame. The cusp arises because in transforming the finite projectile frame DDCS's to the laboratory frame one must divide the DDCS's by k_p, the detached electron's momentum in the projectile frame.[15] At and near threshold, $k_p \approx 0$, which gives rise to the cusp behaviour seen in the laboratory frame results in Fig. 4. The experimental results[14] were measured at 0° in the laboratory with an angular acceptance of 0.506°. As the theoretical results show, the cusp feature is disappearing rapidly as θ_L increases from $\theta_L = 0°$. Thus a convolution of the theoretical results over a finite angular range is necessary for a precise comparison with the experimental results. However, qualitatively, the agreement of theory and experiment regarding this cusp feature is quite good.

The shoulder features on either side of the cusp in both theoretical and experimental results is another earmark of the low–energy states of the H(n=2) – e^- system. These shoulders are due to the $^1P+$ shape resonance shown in Fig. 2 for the related detachment process given in Eq. 9. For angles $\theta_L \lesssim 0.4°$ the kinematic transformation from the projectile to the laboratory frame results in a sampling of the $^1P+$ shape resonace feature twice, once on either side of the so–called equal velocity energy of the detached electron (in which the detached electron travels with the same velocity as the incident H^- projectile). The asymmetry seen experimentally in the relative magnitude of the $^1P+$ shoulder features is not reproduced well by the theoretical calculations and remains a question for future investigations.

Exhibition of Gailitis–Damburg oscillations[11] by studying collisional detachment processes is difficult. In collisional detachment all the final

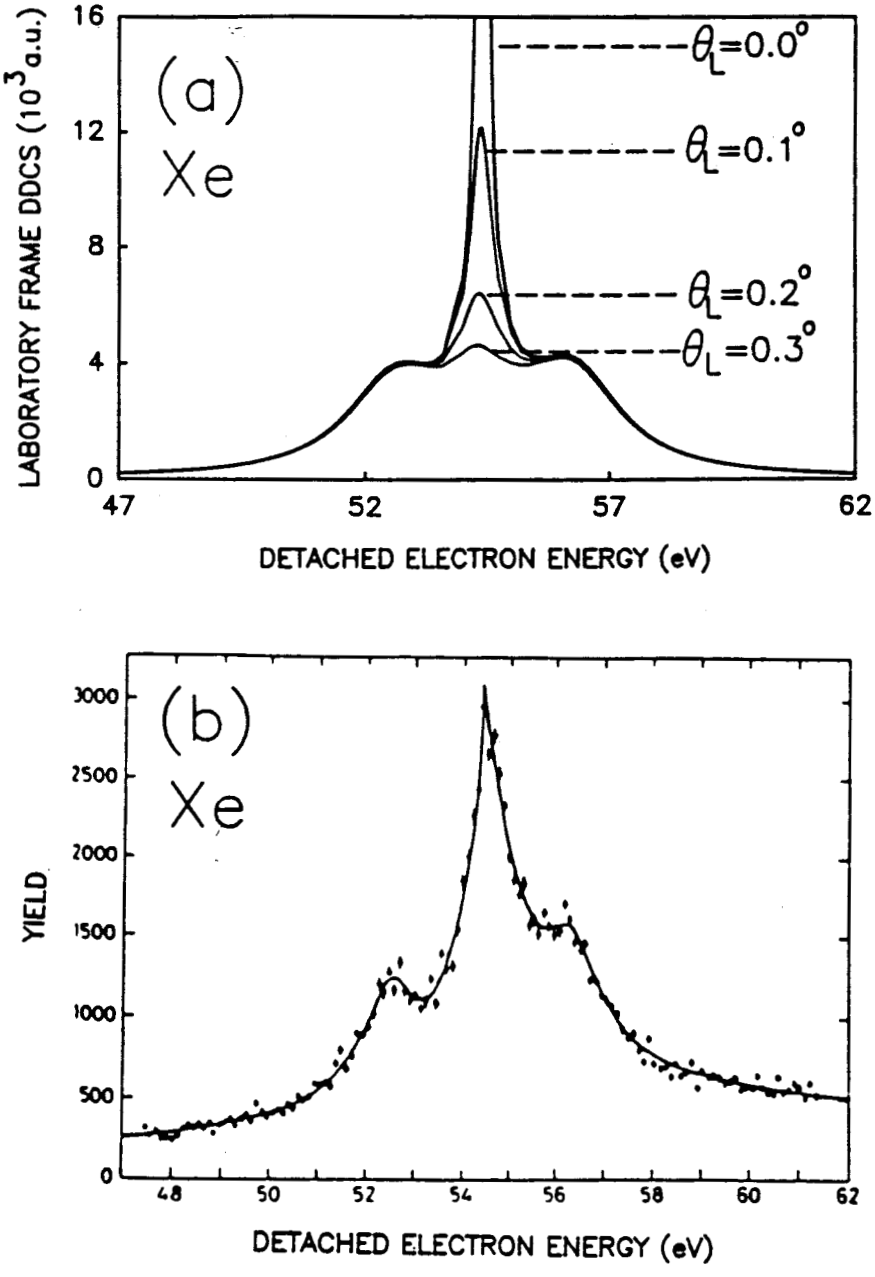

FIG. 4. Laboratory–frame DDCS's for the process 0.1 MeV H^- + Xe → H(n=2) + e^- + Xe*. (a) Theoretical results of Liu and Starace (Ref. 4) for electron detachment angles θ_L = 0.0°, 0.1°, 0.2°, and 0.3°. (b) Experimental results of Andersen, Bangsgaard, and Sørensen (from Ref. 14) for θ_L = 0.0°. The experimental angular acceptance is 0.506°.

state channels are populated. Hence the strong $^1P+$ shape resonance feature dominates the cross sections except for the very narrow energy region near threshold in which the $^1P+$ channel cross section is smaller than those for the channels which have finite threshold cross sections. But in this region, the laboratory frame DDCS has a cusp. Thus another process must be used to make the Gailitis–Damburg oscillations manifest.

4. Photodetachment of H^-

Because of electric dipole selection rules, the photodetachment process in Eq. 2 is a much more selective process than collisional detachment for studying $H(n=2) - e^-$ states. Since the initial state of H^- has ^1S symmetry, photodetachment accompanied by excitation of H(n=2) populates only the three $^1P^o$ final state channels whose effective potentials are shown in Fig. 1, i.e., the $^1P+$, $^1P-$ and $^1P(pd)$ channels.

As discussed in detail by Lin,[8] the $^1P+$ potential is attractive at short distances and weakly repulsive at large distances thereby giving rise to a shape resonance (seen experimentally at about 18 meV above threshold). The $^1P(pd)$ potential is strongly repulsive at all distances. Finally, the $^1P-$ potential is repulsive only at short distances, but is attractive at large distances. This channel has a complex effective angular momentum, λ_μ, and, as discussed above, gives rise to a small but finite cross section at threshold. However, due to the shape resonance near threshold, Gailitis–Damburg oscillations[11] near threshold are obscured. In addition, Gailitis–Damburg oscillations are extremely weak for the $^1P-$ channel.[16] For these reasons, we do not examine the near threshold behavior of the cross section in detail for this process.

The dominant feature of the near threshold photodetachment cross section of H^- is the $^1P+$ shape resonance feature. Our results for the total $n = 2$ cross section, i.e., $\sigma_{2s} + \sigma_{2p}$, are shown in Fig. 5 in comparison with the relative experimental data of Butterfield.[17] As pointed out by Lin,[8] the hyperspherical potential $^1P+$ predicts a shape resonance about 18.9 meV too high. In order to compare our $n = 2$ cross sections with experiment, we have therefore shifted our curves 18.9 meV lower in energy *for this figure only*. The experimental data in Fig. 23 of Ref. 17 have a non–zero back

ground below threshold; we have subtracted this background from the data above threshold. Furthermore, we have normalized the experimental data to our theoretical prediction at the peak of the shape resonance. As shown in Fig. 5, our theoretically predicted n = 2 cross section is somewhat wider in energy than measured experimentally. Nevertheless, the agreement is quite reasonable considering that our final state hyperspherical potentials are uncoupled. Indeed, the adiabatic hyperspherical results appear to be intermediate in accuracy between the three–channel close–coupling results of Hyman, Jacobs, and Burke[18] and the very detailed results for the total cross section of Broad and Reinhardt,[19] as discussed in detail elsewhere.[5]

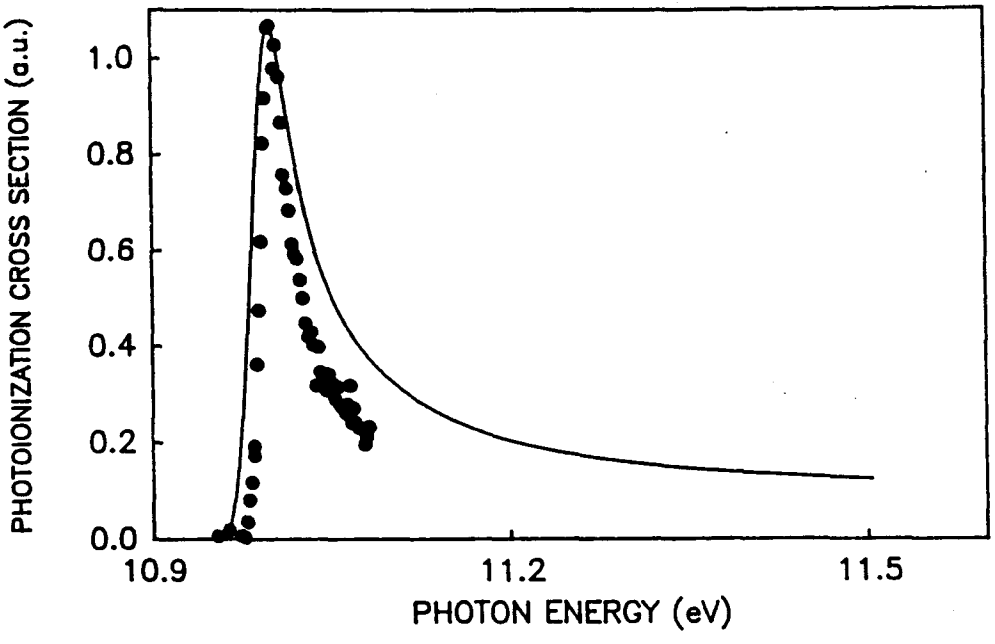

FIG. 5. Photodetachment cross section for the process $\gamma + H^- \rightarrow H(n=2) + e^-$. Solid line: (dipole length) adiabatic hyperspherical results of Liu, Du, and Starace (Ref. 5) shifted to the experimental peak position. Solid circles: relative experimental data of Butterfield (Ref. 17) normalized to the theoretically predicted peak height.

5. Two–Photon Detachment of H^-

The two–photon detachment process in Eq. 3 is a very favorable one for observing Gailitis–Damburg oscillations[11] above the H(n=2) threshold.[5] This is so for two reasons. First, electric dipole selection rules do not permit population of $^1P^o$ final state channels. Hence the strong shape resonance in the $^1P+$ final state channel about 18 meV above threshold cannot obscure these near–threshold oscillations. Second, the two–photon process does populate $^1S^e$ and $^1D^e$ final state channels, one of which, the $^1D+$ channel, is the only one with significant, undamped oscillations above threshold.[5]

Before demonstrating these Gailitis–Damburg oscillations[11] for this process, we must ask how we can be sure that the wiggles our calculations give for the two–photon detachment plus excitation cross sections of H^- are really due to long–range dipole field affects and are not due to some other cause. The answer is that the generalized quantum defect theory (QDT) of Greene, Fano, and Strinati[20] for a long range dipole field enables us to disentangle dipole–field effects from our numerical results analytically. In this way we are able to state with assurance which features of our cross section results are truly the Gailitis–Damburg oscillations[11] and which features are energy–dependent wiggles arising from other causes.

Through use of the QDT for long–range dipole fields,[20] one may show that our adiabatic hyperspherical radial functions, defined by Eq.(5), tend asymptotically to

$$F_{\mu k}(R) \underset{R\to\infty}{\sim} (2/\pi k)^{1/2}\sin(kR + \xi_\mu + \eta_\mu), \tag{12}$$

where η_μ is the phase shift in the μth channel and ξ_μ is an analytic phase dependent on the effective angular momentum λ_μ characterizing the long–range dipole interaction of the H(n=2) – e^- system.[20] For real values of λ_μ,

$$\xi_\mu \equiv -\frac{1}{2}\pi\lambda_\mu \ , \tag{13}$$

while for complex values of λ_μ,[20]

$$\xi_\mu \equiv -\frac{1}{4}\pi + \theta_\mu \ , \tag{14}$$

where (cf. Eq. 8)

$$\theta_\mu \equiv -\tan^{-1}\frac{\tan[\,\alpha_\mu \ln(k/2) + x_\mu\,]}{\tanh(\pi\alpha_\mu/2)} \tag{15}$$

and

$$x_\mu \equiv \arg\Gamma(1 - i\alpha_\mu) \ . \tag{16}$$

The generalized QDT may also be used to extract the long–range dipole–field–induced energy dependence of $F_{\mu k}(R)$ by representing our adiabatic hyperspherical radial wave functions as[21]

$$F_{\mu k}(R) = N_\mu(k)\, \overset{\circ}{F}_{\mu k}(R) \tag{17}$$

where $N_\mu(k)$ is an effective normalization factor an which determines essentially all of the energy dependence of the radial wave function near $R \approx 0$, and where $\overset{\circ}{F}_{\mu k}(R)$ is a more smoothly varying function of k. The oscillatory, energy–dependent normalization factor $N_\mu(k)$ is an analytically known function of ln k.[5,21]

There are two ways in which an attractive dipole field introduces oscillations in measured cross sections on a ln k energy scale. The first is due to the rapid variation of the analytically determined dipole phase θ_μ (cf. Eqs. 14 and 15) for those hyperspherical channels μ having complex values of the effective angular momentum λ_μ. This analytically determined phase θ_μ (through ξ_μ) appears explicitly in the phase factor included in the two–photon transition amplitudes.[5] Interference effects between different

amplitudes, such as occur commonly in calculating the angular distributions for the detached electrons, generally lead to sizable, undamped oscillations in the corresponding cross sections due to the rapid decrease of the analytically determined phases θ_μ with increasing ln k. This analytic behavior is shown in Fig. 6 for all three channels having complex λ_μ above the H(n=2) threshold.

The second way the long–range dipole field introduces oscillations in the cross sections is through the effective normalization $N_\mu(k)$ introduced in Eq. 17. Its behavior is shown in Fig. 7 for each of the three channels above the H(n=2) threshold having complex λ_μ. One sees clearly that whereas the long–range dipole–field–induced oscillations of $N_\mu(k)$ for the $^1S(K = +1)$ and $^1P-$ channels are strongly damped, those for the $^1D+$ channel are quite sizable.[5]

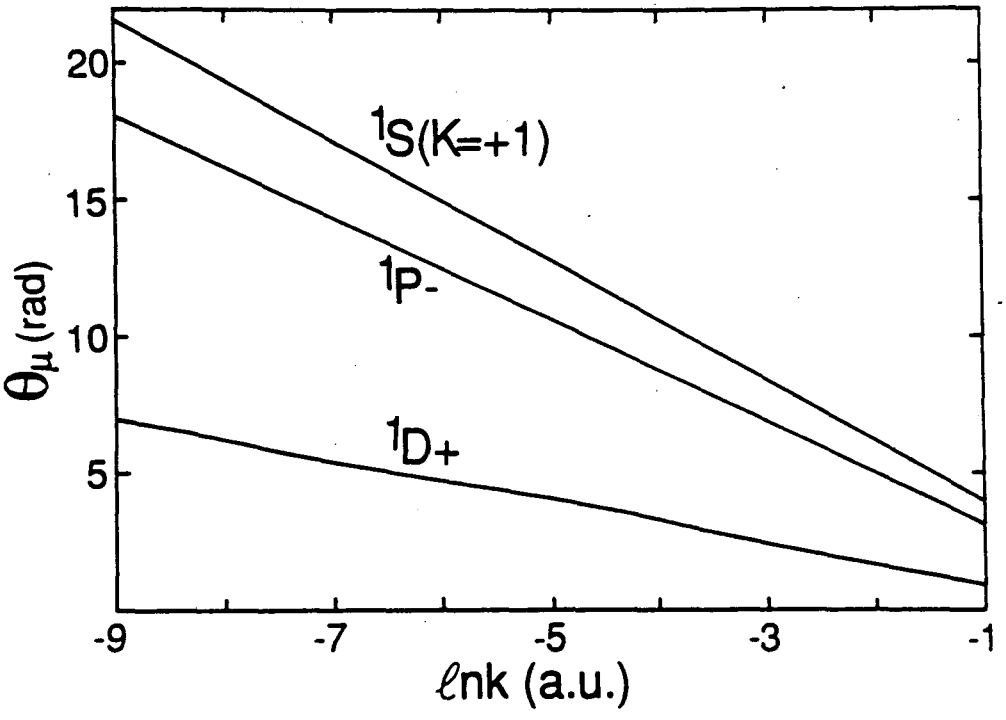

FIG. 6. Analytic phase θ_μ [defined in Eq. 15] vs lnk, where k (a.u.) is the detached–electron momentum, for the three adiabatic hyperspherical channels $\mu = {}^1S(K = +1)$, $^1P-$, and $^1D+$.

The total cross sections for the two–photon detachment of H^- with excitation of H(n=2) (cf. Eq. 3) are given for the cases of linearly (L) and circularly (C) polarized light in Figs. 8(a) and 8(b) respectively. In Figs. 8(c) and 8(d) we have used the generalized QDT[20,21] to extract analytically the energy–dependence arising from the long–range dipole field in order to give renormalized cross sections.[5] One sees clearly that for electron momenta such that $\ln k \lesssim -3.0$, the oscillations of the cross sections are due to the long–range dipole field. Now, for $\ln k \lesssim -6.0$, the assumed degeneracy of H(2s) and H(2p) breaks down due to spin–orbit and Lamb shift effects. Thus, for $-6.0 \leq \ln k \leq -3.0$ or, alternatively, for detached electron kinetic energies from ≈ 0.1 meV to ≈ 34 meV, the energy dependence of the cross sections may be ascribed to Gailitis–Damburg oscillations.[11] As shown in Figs. 8(a) and 8(b), this energy region corresponds to a half–cycle of such oscillation over which the L cross section increases by ≈ 30% and the C cross section increases by ≈ 50%.

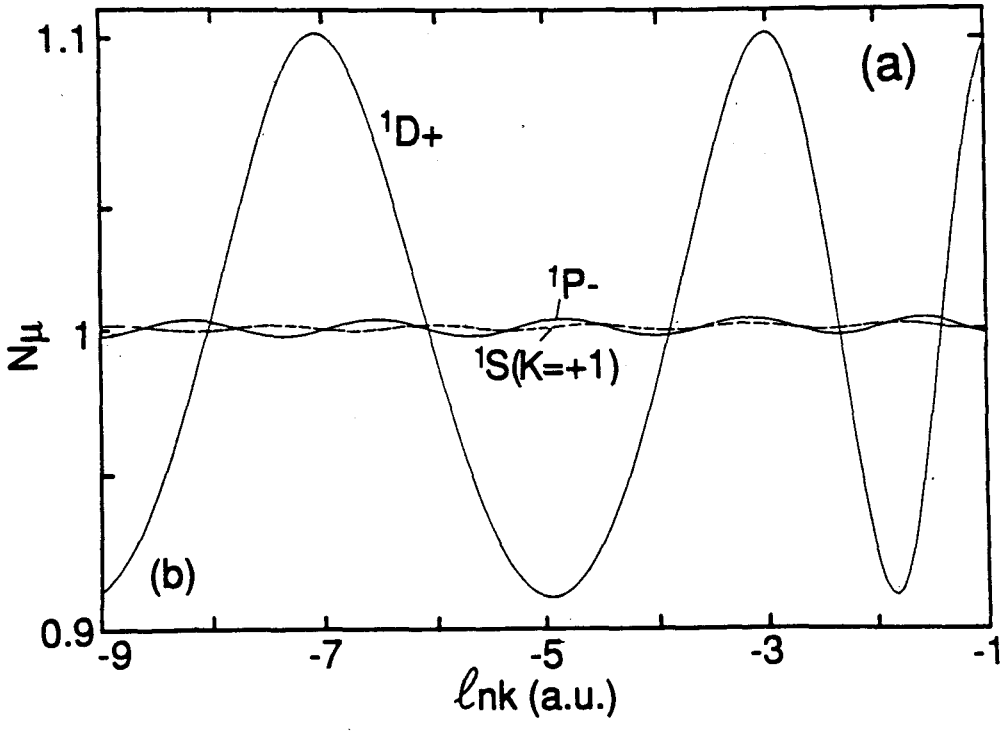

FIG. 7. Normalization factors $N_\mu(k)$ [cf. Eq. 17] for the three adiabatic hyperspherical channels $\mu = {}^1S(K = +1)$, ${}^1P-$, and ${}^1D+$ vs ln k, where k is the detached–electron momentum.

In Fig. 9 we present our results[5] for the total n = 2 differential cross section, which is the sum of the differential cross sections for the 2s and 2p states. Results are given for the six angles, θ_k = 0°, 18°, 36°, 54.7°, 72°, and 90°. [Note that the results labelled θ_k = 54.7° are actually calculated for θ_k = 54.7356°, at which $P_2(\theta_k) = 0$.] One sees from this figure that the energy dependence of the differential cross section in the region $-6 \lesssim \ln k \lesssim -3$ (over which long–range dipole field effects play the major role) is highly dependent on the angle θ_k at which the photoelectron is detected. This energy dependence may be enhanced by use of linearly polarized light and small angles of detection, θ_k.

Note that the energy–dependences of the total two–photon detachment cross sections presented in Fig.8 are governed primarily by the long range dipole field normalization factors $N_\mu(k)$ (Cf. Fig. 7). The differential cross sections in Fig. 9 are strongly influenced in addition by the rapidly decreasing analytic phases θ_μ (Cf. Fig. 6). Indeed the energy–dependence of the

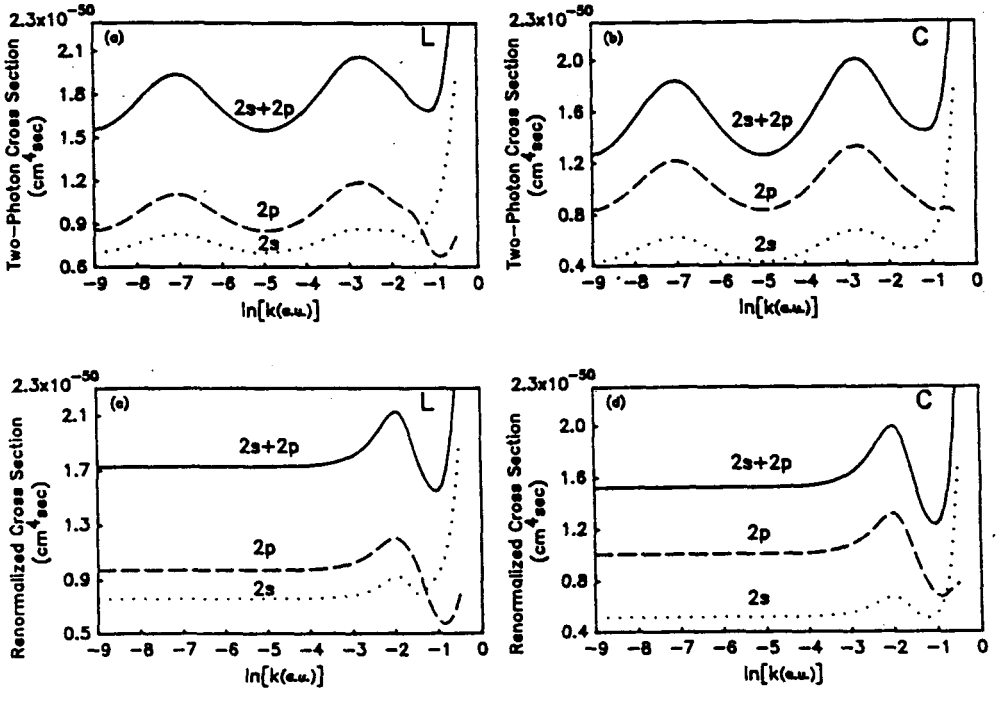

FIG. 8. Generalized two photon cross sections for the cases of linearly (L) and circularly (C) polarized light for the process $2\gamma + H^- \rightarrow H(2s,2p) + e^-$ plotted vs. ln k, where k(a.u.) is the photoelectron momentum. (a) L results; (b) C results; (c) renormalized L results; (d) renormalized C results.

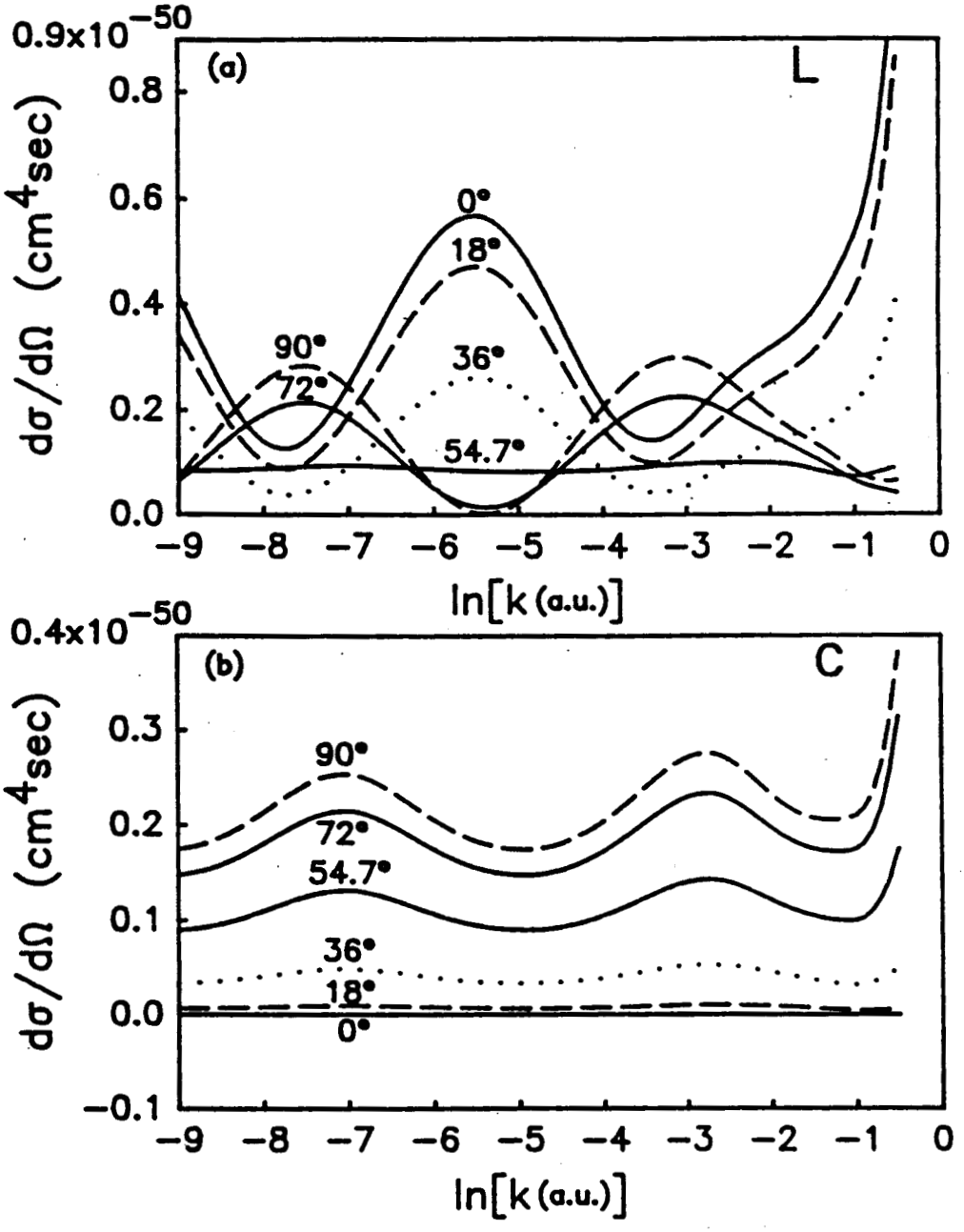

FIG. 9. Differential cross sections for the cases of linearly L and circularly (C) polarized light for the process $2\gamma + H^- \rightarrow H(n=2) + e^-$ plotted vs. ln k, where k(a.u.) is the photoelectron momentum, for the detached electron angles θ_k = 0°, 18°, 36°, 54.7356°, 72°, and 90°. (a) L results; (b) C results.

asymmetry parameters for the two–photon process (Cf. Ref. 5) is primarily governed by these analytic phases. Thus, the long–range dipole field effects due primarily to $N_\mu(k)$ can be found by measuring the total cross sections, while those due primarily to θ_μ can be found by measuring the angular distribution asymmetry parameters.[5]

6. Conclusions

In this paper we have shown how the low–energy states of the fundamental H(n=2) – e^- three–body system influence three very different processes for detaching the H^- ion. We have also shown that these three different detachment processes are each best suited to make manifest a different one of the properties of the long–range dipole field interactions within the H(n=2) – e^- system. Thus, collisional detachment of H^- with measurement of the detached electron in the forward direction is best suited for demonstrating the finite threshold cross sections of those channels which have an attractive dipole–field interaction at asymptotic distances. This is so because the kinematic transformations from the projectile frame to the laboratory frame lead to a cusp behavior in the laboratory frame DDCS's which is possible only because of the finite threshold cross sections in the projectile frame.

Single photon detachment of H^- with excitation of H(n=2) is ideal for observing the shape resonance feature in one of the $^1P^o$ final state channels above the H(n=2) threshold. Electric dipole selection rules result in only final state channels having $^1P^o$ symmetry. The $^1P+$ channel, in which the shape resonance occurs, has a cross section so much larger than those for other allowed $^1P^o$ channels that the shape resonance feature can be observed very clearly.

Finally, the two–photon detachment of H^- with excitation of H(n=2) is the most likely process in which to observe the long–range dipole–field–induced oscillations above threshold that were predicted by Gailitis and Damburg[11] but which have yet to be observed experimentally in any process. On the one hand, the $^1P^o$ shape resonance feature is not populated in this process, and hence cannot obscure these oscillations. On the other hand, the $^1D+$ final–state channel which is populated has the largest amplitude for such oscillations of any final state channel. Theoretical calculations[5] predict a half cycle of such oscillation over the energy region from 0.1 meV to about 34 meV above threshold.

7. Acknowledgment

This work was supported in part by the U.S. Department of Energy, Office of Basic Energy Sciences, Division of Chemical Sciences, under Grant No. DE–FG02–88ER13955.

8. References

1. J. Macek, J. Phys. B **1** (1968) 831.
2. C.R. Liu and A.F. Starace, Phys. Rev. Lett. **62** (1989) 407.
3. C.R. Liu and A.F. Starace, Phys. Rev. A **40** (1989) 4926.
4. C.R. Liu and A.F. Starace, Phys. Rev. A **42** (1990) 2684.
5. C.R. Liu, N.Y. Du, and A.F. Starace, Phys. Rev. A **43** (1991), in press.
6. U. Fano, Rep. Prog. Phys. **46** (1983) 97.
7. A.F. Starace, in Fundamental Processes of Atomic Dynamics, edited by J.S. Briggs, H. Kleinpoppen, and H.O. Lutz (Plenum, New York, 1988), pp 235–258.
8. C.D. Lin, Phys. Rev. Lett. **35** (1975) 1150.
9. M.J. Seaton, Proc. Phys. Soc. (London) **77** (1961) 174.
10. C. Greene, U. Fano, and G. Strinati Phys. Rev. A **19** (1979) 1485.
11. M. Gailitis and R. Damburg, Zh. Eksp. Teor. Fiz. **44** (1963) 1644 [Sov. Phys. JETP **17** (1963) 1107], and Proc. Phys. Soc. London **82** (1963) 192; M. Gailitis, in *Atomic Physics 6*, edited by R. Damburg and O. Kukaine (Plenum, NewYork, 1978), pp. 249–266.
12. C.D. Lin, Phys. Rev. A **29** (1984) 1019; Adv. At. Mol. Phys. **22** (1986) 77. Specifically, our channels μ converging to the H(n=2) level have the following labels in Lin's $(K,T)^A$ notation: $^1S(K = \pm 1)$: $(\pm 1,0)^+$; $^1P+$: $(0,1)^+$; $^1P-$: $(1,0)^-$; $^1P(pd)$: $(-1,0)^0$; $^1D+$: $(1,0)^+$.
13. M.M. Duncan and M.G. Menendez, Phys. Rev. A **16** (1977) 1799.
14. L.H. Anderson, J.P. Bangsgaard, and J. Sørensen, Phys. Rev. Lett. **57** (1986) 1558.
15. See, e.g., Eq. (44) of Ref. 3.
16. C.H. Greene and A.R.P. Rau, Phys. Rev. A **32** (1985) 1352.
17. Kenneth B. Butterfield, The University of New Mexico, Ph.D. Thesis (Los Alamos National Laboratory Thesis No. LA–10149–T, 1984), Sec. IV. Values for the n = 2 cross section in Fig. 23 appear on pp. 124–5.
18. H.A. Hyman, V.L. Jacobs, and P.G. Burke, J. Phys. B **5** (1972) 2282.
19. J.T. Broad and W.P. Reinhardt, Phys. Rev. A **14** (1976) 2159.
20. C. Greene, U. Fano, and G. Strinati, Phys. Rev. A **19** (1979) 1485.
21. U. Fano and A.R.P. Rau, Atomic Collisions and Spectra (Academic, New York, 1986), Secs. 5.4 and 5.7.3.